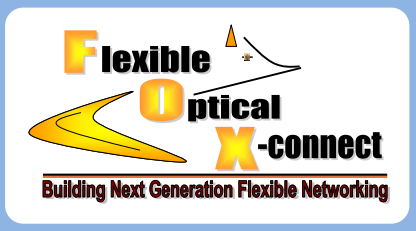

PROJECT: **FOX-C** CONTRACT NO.: **318415**
FLEXIBLE OPTICAL CROSS-CONNECT NODES
ENABLING NEXT-GENERATION FLEXIBLE OPTICAL NETWORKING

SPECIFIC TARGETED RESEARCH PROJECT (STREP)
INFORMATION & COMMUNICATION TECHNOLOGIES (ICT)

Document Type: Deliverable

Dissemination Level: RE

D4.3

Report on the design and implementation of elements for the 'drop' function of the node

Lead beneficiary: Hebrew University

Contact person: Dan Marom

Address: Applied Physics Department, Hebrew University, Jerusalem, ISRAEL

Email: danmarom@mail.huji.ac.il, Tel.:+97226584851

Date due of delivery: 31/03/2014

Submission date: 10/07/2014

Contributing institutes: HUJI, Finisar, ASTON

Authors: Dan Marom (HUJI), StylianosSygletos (Aston), Andrew Ellis (Aston), Shalva Ben-Ezra (Finisar).

This document has been prepared in compliance of Deliverable 4.3 for FP7-ICT project FOX-C and reports on the design and implementation of the 'drop'elements realized for the hierarchical ROADM node, where a super-channel is first dropped from the fiber level and then signal tributaries or sub-channels are selected from within.

Revision History

No.	Version	Author(s)	Date
1	1.0	Dan Marom (HUJI)	**01/06/14**
	Comments:	**V. 1, combining information from multiple sources**	
2	1.1	José Manuel Rivas (AIT)	**04/07/14**
	Comments:	**Internal Review**	
3	1.2	Dan Marom (HUJI)	**04/07/14**
	Comments:	**Accepted comments. Added summary table in the end**	
4	1.3	Jordi Ferre Ferran (WONE)	**06/07/14**
	Comments:	**Internal review**	
5	1.4	Dan Marom (HUJI)	**09/07/14**
	Comments:	**Accepted comments. Added definition of optical resolution and spectral addressability. Final version**	
6			
	Comments:		
7			
	Comments:		
8			
	Comments:		
9			
	Comments:		
10			
	Comments:		
11			
	Comments:		
12			
	Comments:		
13			
	Comments:		
14			
	Comments:		
15			
	Comments:		

Table of Contents

Revision History 1
Table of Contents 2
Table of Figures 3
Executive Summary 5
1 Introduction – The FOX-C Hierarchical ROADM Node Design 6
2 Switching Super-Channels at the Fibre Link Level 8
2.1 Flexible-Grid Wavelength-Selective Switches 8
2.2 WSS graphical user interface 9
3 Switching and Filtering Sub-Channels within the Super-Channel Level 11
3.1 AWG Phase Error Trimming Using Intense UV Laser Irradiation 13
3.2 AWG Phase Error Correction With a Spatial Light Modulator 17
3.3 Bulk Grating based Fine Resolution Filter 22
4 Conclusions 25

Table of Figures

Figure 1.1 – FOX-C information flow at three levels: Super-channels for transport at the fibre link level, tributary de/recomposition at the single super-channel level, and tributary handling (e.g. detection, switching, and transmission) at the band/channel level. The ROADM components and functionality are described in this document. 6
Figure 1.2 – Definition of optical resolution and spectral addressability in the filtered channel response. The optical resolution determines the roll-off shape from pass-band to block-band. The spectral addressability is the placement resolution of the filter edge. 7
Figure 2.1 – Left: Finisar WSS design, employing free-space optics and an LCoS switching engine. Right: FOX-C prototype WSS offering 20 output fibre ports, flex-grid operation, and 7.5 GHz optical resolution. 9
Figure 2.2 – FOX-C flexible bandwidth measured spectral characteristics. Left: flexible pass bandwidth. Right: flexible notch bandwidth. 9
Figure 2.3 – FOX-C super-channel Add/Drop based on a dual WSS arrangement, where one is used to distribute the incoming channel across the drop ports and the other for aggregating the channels towards the line side. 10
Figure 2.4 – FOX-C super-channel Add/Drop based on a dual WSS arrangement, where one is used to distribute the incoming channel across the drop ports and the other for aggregating the channels towards the line side. 10
Figure 2.5 – FOX-C elastic channel definition panel, allowing each spectral slot to be individually addressed. 11
Figure 3.1 – AWG design and implementation for FOX-C. 200 GHz FSR and 250 waveguides should provide <1 GHz optical resolution, provided the AWG is devoid of phase errors. 12
Figure 3.2 – Measured phase errors of 250 waveguide arms of high resolution AWG. 13
Figure 3.3 – Layout of the AWG phase error evaluation system and UV trimming. The UV beam scans along the waveguide arms and can expose each WG to a dose required to adjust the phase at the output. ... 13
Figure 3.4 – Experimental phase trimming data. Top row:Phase shift as a function of energy exposure. Left shows photosensitivity phase shift; Right shows stress phase sensitivity. Bottom left: Image of WG (straight line) after photosensitivity trimming (image identical to untrimmed WG). Bottom right: Image of WG after stress trimming (visible due to deformation of PLC's surface)..... 15
Figure 3.5 –Polarization-dependent phase trimming. Left: Horizontal polarization. Right: Vertical polarization. Bottom: Surface profile after trim obtained by Dektak profilometer. 16
Figure 3.6 – AWG phase trimming results. Top row: Directly after trimming session; output phase errors are nearly uniform and we witness the far field radiation constructively focusing. Bottom row: After two weeks; output phases drift and far field radiation pattern is broadened..... 17
Figure 3.7 – Experimental setup for compensation of AWG phase errors with an LCoS phase modulator and spectral processing in the Fourier plane. 18
Figure 3.8 – The placement of the camera in the experimental setup for locating WGs and conducting interference between adjacent WGs. 19
Figure 3.9 – Waveguides at the image plane. Left: Direct image of the waveguide array. Right: Identification of the WG positions by column scanning across the array. Correspondence with image is apparent (identified by dead waveguides). 19
Figure 3.10 – Left: Image plane illustration of two adjacent waveguides tilted on the SLM to direct the light from only those two WG, while one has an applied phase offset.Right: Photo of two in phase waveguides.Center: A vertical sum of the image intensity on the camera. 20

Figure 3.11 – Left: All WG phases compared to a middle WG in gray scale.Right: The color-coded HDTV image frame sent to the SLM (actual values are greyscale) to phase synchronize the AWG. Colors (from blue to red) represent greyscale values from 0 to 255. 20
Figure 3.12 – Measured fine spectral filter performance characteristics, when variable bandwidth channels are deployed at spectral granularity of 100 MHz and a record optical resolution of 0.8 GHz. .. 21
Figure 3.13 – Top view of experimental system for fine resolution optical filtering using the dual LCoS approach..... 21
Figure 3.14 – Expected diffraction efficiency of Echelle grating operating in 40th order. 22
Figure 3.15 – High resolution filter, employing blazed Echelle grating for high resolution dispersion and an LCoS switching engine. The LCoS SLM can be reprogrammed to allocate optical channel bandwidths differently at quanta determined by the spectral granularity. 23
Figure 3.16 – The ZEMAX optical system simulations. A.Rays from a single input fiber to the SLM, B. Rays from the SLM to a single output fiber.Bottom: Coupling performance evaluated for each polarization. 24

Executive Summary

In this report we describe the design and implementation of the 'Drop' elements of the hierarchical ROADM node within the FOX-C project. The hierarchical approach allows to efficiently utilize the optical communication bandwidth by employing super-channel transport on the fiber and extraction of individual sub-channels at add/drop nodes without the need to deploy a full super-channel receiver.

Filtering elements are an integral component throughout the ROADM node, first to select individual super-channels from the fiber transport level, and subsequently to optically drop sub-channels or shape signals at very fine resolution and precision. The fiber transport level super-channel selection is performed with a custom wavelength-selective switch (WSS) made by project partner Finisar. This WSS provides optical resolution of 7.5 GHz and spectral addressability of 6.25 GHz, which allow for flexible terabit super-channel routing and selection at the ROADM node. The WSS is fully packaged in industry-compliant enclosure, supporting several interfaces. For the FOX-C implementation, custom operating software running on a PC and interfacing the WSS via USB cable has been prepared. The software enables spectral band selection to any one of the 20 fiber output ports, at up to 5dB loss.

At the sub super-channel level, a fine resolution spectral processor has been implemented by project partner HUJI. The processor is based on an arrayed waveguide grating (AWG) providing sub-1GHz optical resolution over a 200 GHz-wide contiguous bandwidth window. Due to extreme sensitivity of this AWG to fabrication and stress-related phase errors, two techniques have been developed in an attempt to compensate these errors. The first technique is based on phase trimming with a UV laser but the results to date have not been stable enough or scalable to the waveguide count of the AWG. The second technique is based on active compensation with a spatial light modulator (SLM) operating in reflection mode and assigning additional fixed phases for proper operation. With the second technique, the processor provides 0.8 GHz optical resolution and spectral addressability of 100 MHz over the 200 GHz wide window, allowing for arbitrary sub-channel extraction at record edge sharpness. The processor is interfaced to a laptop controlling the two liquid-crystal on silicon (LCoS) SLM (the first for correcting the phase values and the second for the spectral manipulations) via video drivers operated by custom Matlab code. The processor insertion loss is 16dB, which is quite high for the application but can be compensated by additional amplification at the ROADM node. As an alternative lower-loss spectral processor, partner HUJI is currently preparing in parallel a large bulk diffraction grating based WSS, conforming to nearly the same spectral resolution (~1.5 GHz).

These two FOX-C prototypes for the 'Drop' elements, jointly prepared under D4.2, will be incorporated next in system experiments implementing the full ROADM node functionality.

1 Introduction –The FOX-C Hierarchical ROADM Node Design

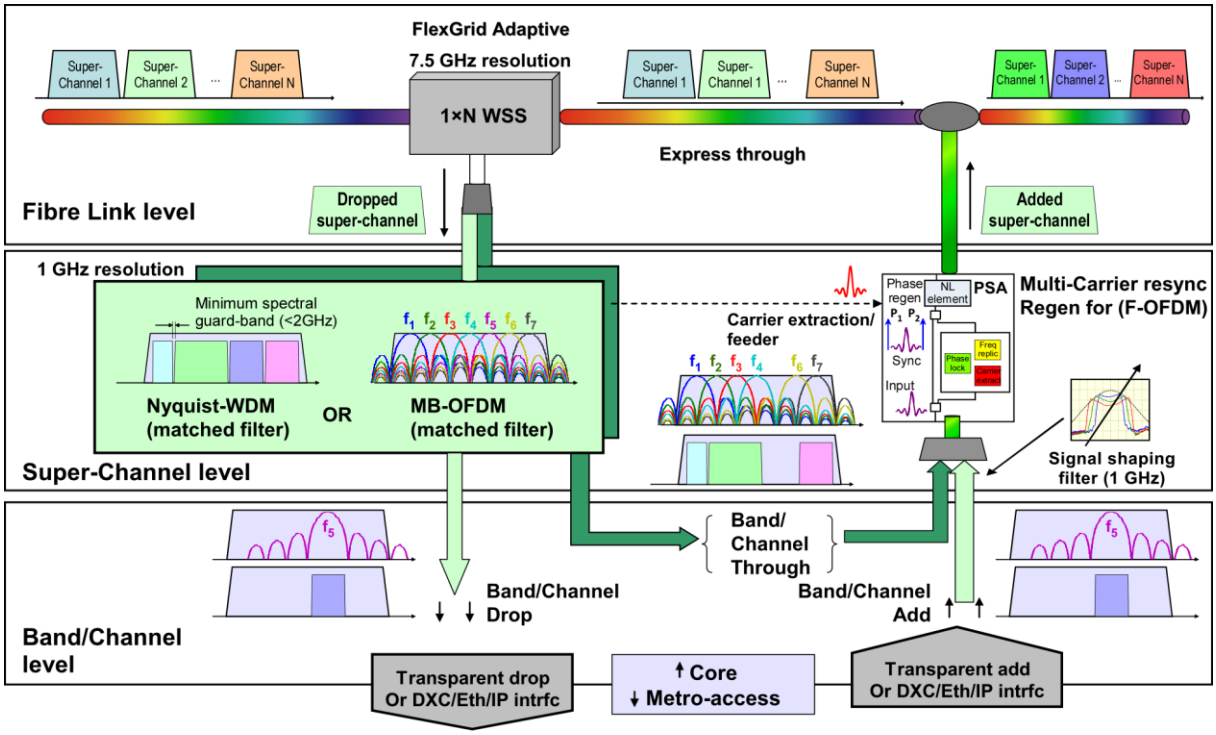

Figure 1.1 – FOX-C information flow at three levels: Super-channels for transport at the fibre link level, tributary de/recomposition at the single super-channel level, and tributary handling (e.g. detection, switching, and transmission) at the band/channel level. The ROADM components and functionality are described in this document.

The FOX-C network concept requires the design and development of adaptive flexible and multi-granular nodes (i.e. a novel flexible ROADM extended to a flexible OXC), which will be the technology enabler for a true flexible optical network. The flexible node of the FOX-C project is an advanced version of ROADM able to handle (i.e. add, drop and pass-through) low granularity bands of sub-carrier channels extracted from and added to Tb/s super-channels in the core. This is addressed in a hierarchical topology (see Figure 1.1), providing the following functionality:

→**At the fibre link level** and from a number of high capacity (up to 1Tb/s) super-channels in the core with flexible spectral characteristics, a WSS can select one super-channel that contains the band channels to be dropped locally. The rest of the super-channels continue directly to the output port. Until this point the function of the node is similar to a typical DWDM ROADM but with a finer adaptation to a variable spectral range and not to a fixed grid (e.g. 100GHz or 50GHz band) as in DWDM. By allocating super-channel bandwidths in an elastic manner with the WSS, the overall fibre bandwidth is optimally utilized.

→**At the super-channel level and the drop section** of the FOX-C node, the extracted super-channel is subdivided into variable bandwidth bands for either drop or express pass-through. This differs from the conventional spectral filtering process, used for DWDM channel processing, because of the overlapping properties of the orthogonal subcarriers in frequency domain for the case of OFDM or the inability to provide sharp edge filtering and separation for the case of Nyquist-FDM. Therefore, for the OFDM-based multi-band schemes, matched filtering conditions are required for the clear extraction (i.e. both drop and erase), while for the Nyquist-FDM scheme, an optimum combination of ultra-fine filter selectivity with minimum guard band requirements is needed. In both cases the fine sub-superchannel selector elements must be bandwidth adaptable to the spectral width of the bands. Therefore a fine resolution (1GHz) adaptive optical filter is required, allowing the detailed design of the filter response function.

Both 'Drop' elements offer the ability to switch and filter an optical signal within the telecommunications band. The two switches differ primarily in their spectral resolving characteristics, with the fibre-link level WSS offering a resolution and spectral addressability conforming to DWDM super-channel selection and the super-channel level fine spectral filtering offering the capability to select sub-channels from within. It is important to distinguish these two spectral metrics (see Figure 1.2); The optical resolution of the 'Drop' element determines the transition bandwidth, ν_{res}, between the pass-band (measured at 90% of peak or -0.5 dB) and the block-band (measured at 10% of peak or -10 dB). The spectral addressability, $\nu_{address}$, is the accuracy at which the filter edge can be placed.

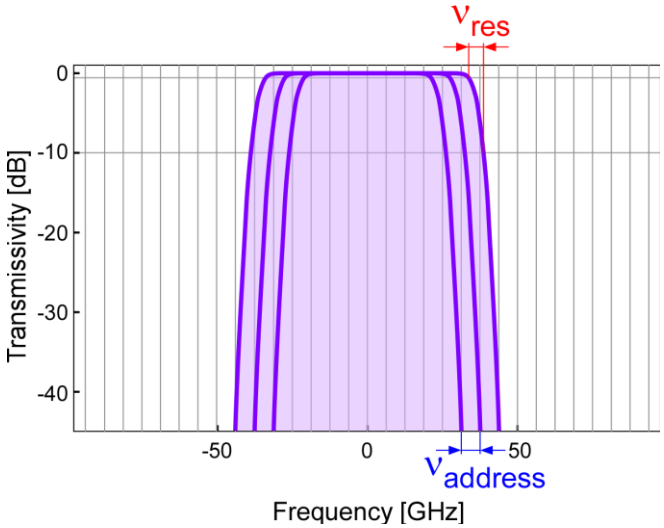

Figure 1.2 – Definition of optical resolution and spectral addressability in the filtered channel response. The optical resolution determines the roll-off shape from pass-band to block-band. The spectral addressability is the placement resolution of the filter edge.

The 'Drop' elements for the FOX-C ROADM node have been developed over the project's first 18 months, implementing a wavelength-selective switch (WSS) to route and drop super-channels of variable overall bandwidth at the fibre-link level and a fine spectral processor

capable of optically filtering the super-channel at sub-channel granularity. These two FOX-C developments jointly comprise deliverable D4.2, *prototypes of flexible elements for the 'drop' function of the node*, and this supporting Report (known as D4.3) describes the design and implementation of these 'Drop' elements. The fiber-link level WSS extracting complete super-channels is discussed in Chapter 2, and the sub-super-channel switching and filtering processor is described in Chapter 3.

2 Switching Super-Channels at the Fibre Link Level

2.1 Flexible-Grid Wavelength-Selective Switches

Finisar is the market leader in WSS technology, achieving this position with its adoption of liquid-crystal on silicon (LCoS) spatial light modulator (SLM) technology as the spectral switching engine. The software re-assignment capability of the LCoS pixels enabled the formation of a new category of flexible-grid WSS. In a flex-grid WSS, the channel position and width become programmable, assigning contiguous small SLM pixel groups to different channels. The individual pixel extent by which specific channels are defined dictates the spectral granularity at which passbands can be configured. The dispersive optical elements determine the spectral resolution, which is manifest by the transition bandwidth from pass to block levels. A prototypical Finisar implementation of its LCoS-based WSS is depicted in Figure 2.1-left. This design has been modified for FOX-C specifications, offering a 7.5 GHz optical resolution, spectral addressability of 6.25 GHz, 20 output ports and an insertion loss of ≤5 dB. The entire WSS is packaged inside an industry standard hermetic enclosure with a variety of electrical interfaces (Figure 2.1-Right). For the FOX-C experimental operation, a custom graphical user interface (GUI) has been written to provide full reprogrammability of the WSS, communicating to the WSS via a USB connection. Details of the GUI interface are shown in the next subsection.

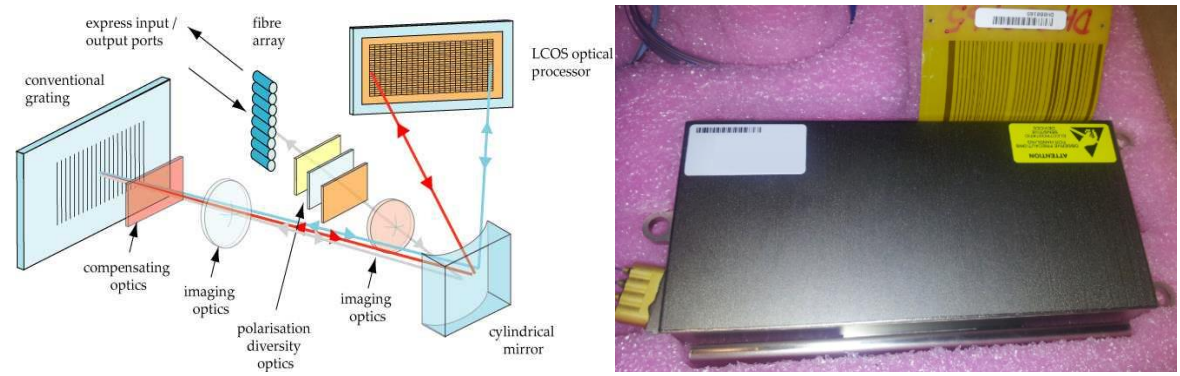

Figure 2.1 – Left: Finisar WSS design, employing free-space optics and an LCoS switching engine. Right: FOX-C prototype WSS offering 20 output fibre ports, flex-grid operation, and 7.5 GHz optical resolution.

The FOX-C WSS was characterized with a LUNA optical vector analyzer (a swept laser interferometer system) for its spectral switching performance, by specifying varying channel pass bandwidth and notch bandwidths, to confirm optical resolution. The WSS is compliant for FOX-C fiber link level switching.

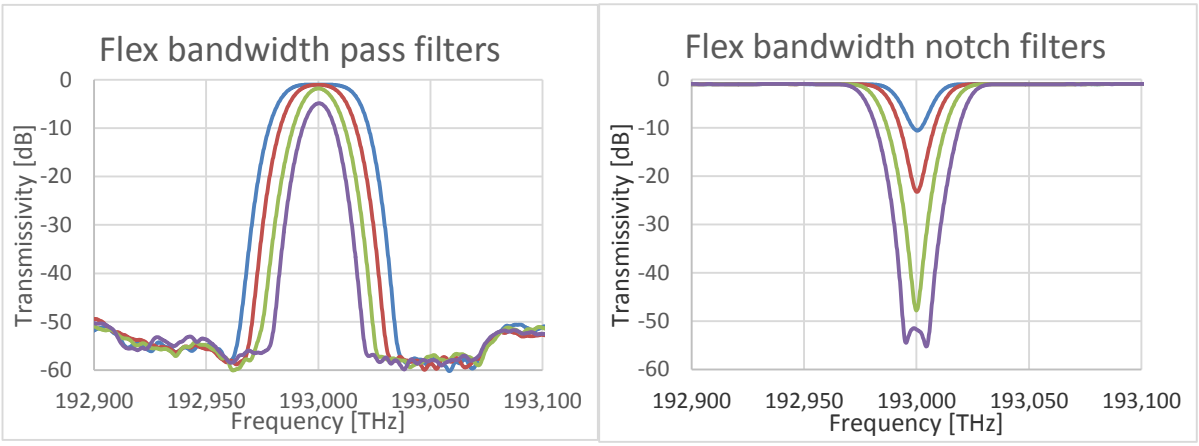

Figure 2.2 – FOX-C flexible bandwidth measured spectral characteristics. Left: flexible pass bandwidth. Right: flexible notch bandwidth.

2.2 WSS graphical user interface

For the FOX-C project, Finisar prepared a custom, LabView-based GUI to control the fiber-level switching at the ROADM node. The ROADM node design has been defined in MS18, and is shown in Figure 2.3. The GUI displays and allows the user to set the switching states of the Add and Drop WSS (see Figure 2.4).The ROADM node also implements monitoring photodiodes before and after each optical amplifier and on the add channels, as well as an optical channel monitor (OCM). The GUI allows the user to define the utilized DWDM grid (e.g., 100GHz and 50 GHz) through state controls.

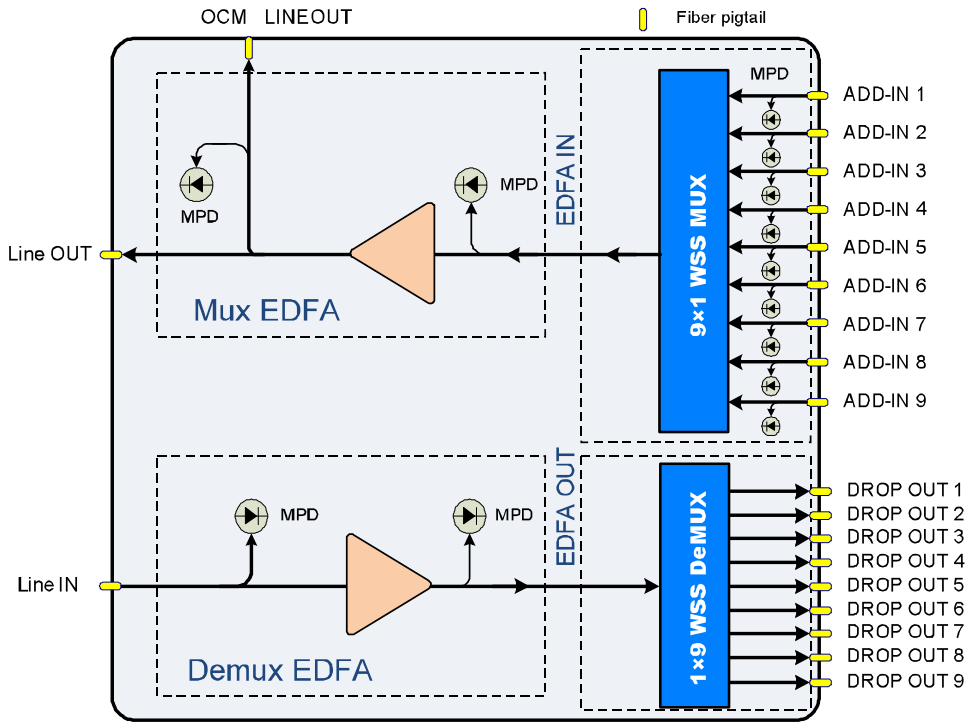

Figure 2.3 – FOX-C super-channel Add/Drop based on a dual WSS arrangement, where one is used to distribute the incoming channel across the drop ports and the other for aggregating the channels towards the line side.

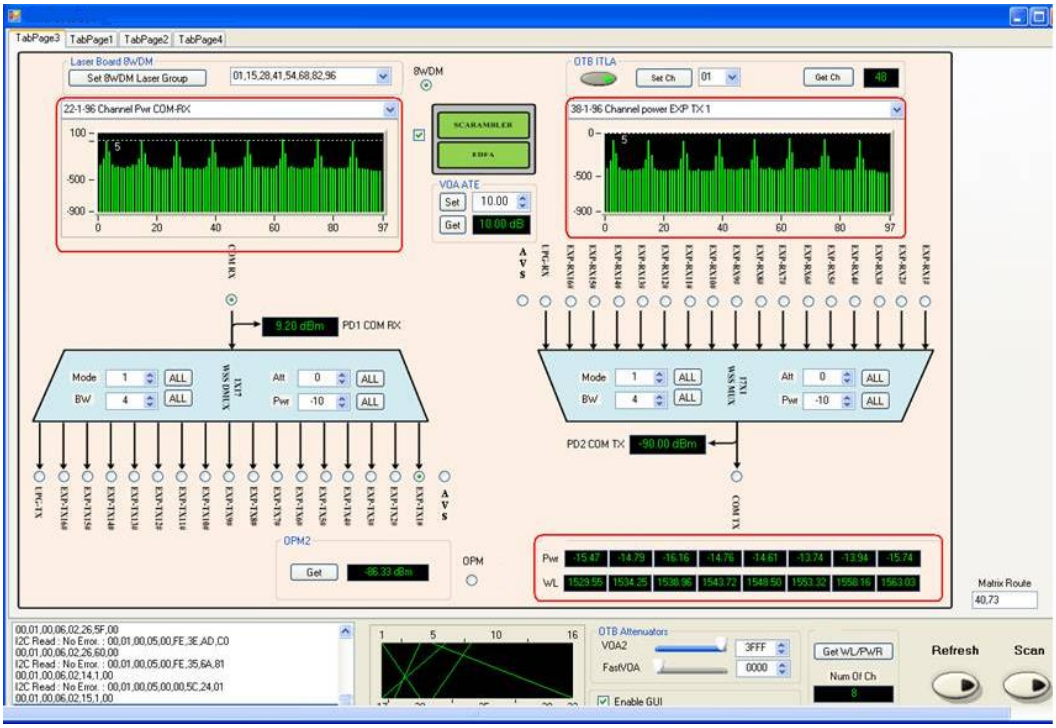

Figure 2.4 – FOX-C super-channel Add/Drop based on a dual WSS arrangement, where one is used to distribute the incoming channel across the drop ports and the other for aggregating the channels towards the line side.

A key distinguishing feature of FOX-C is the support for elastic channel definition, allowing DWDM channels to be arbitrarily placed within the C-band and have individual, user defined

bandwidth. In such an elastic scenario, the WSS channel needs to be defined on a column by column basis (the WSS spectral addressability). In support of the elastic channel definition, an auxiliary GUI panel has been defined, which allows each spectral slot to be assigned to a particular port. While these settings may be cumbersome to hand configure (as shown in Figure 2.5), the settings can also be read from a configuration file.

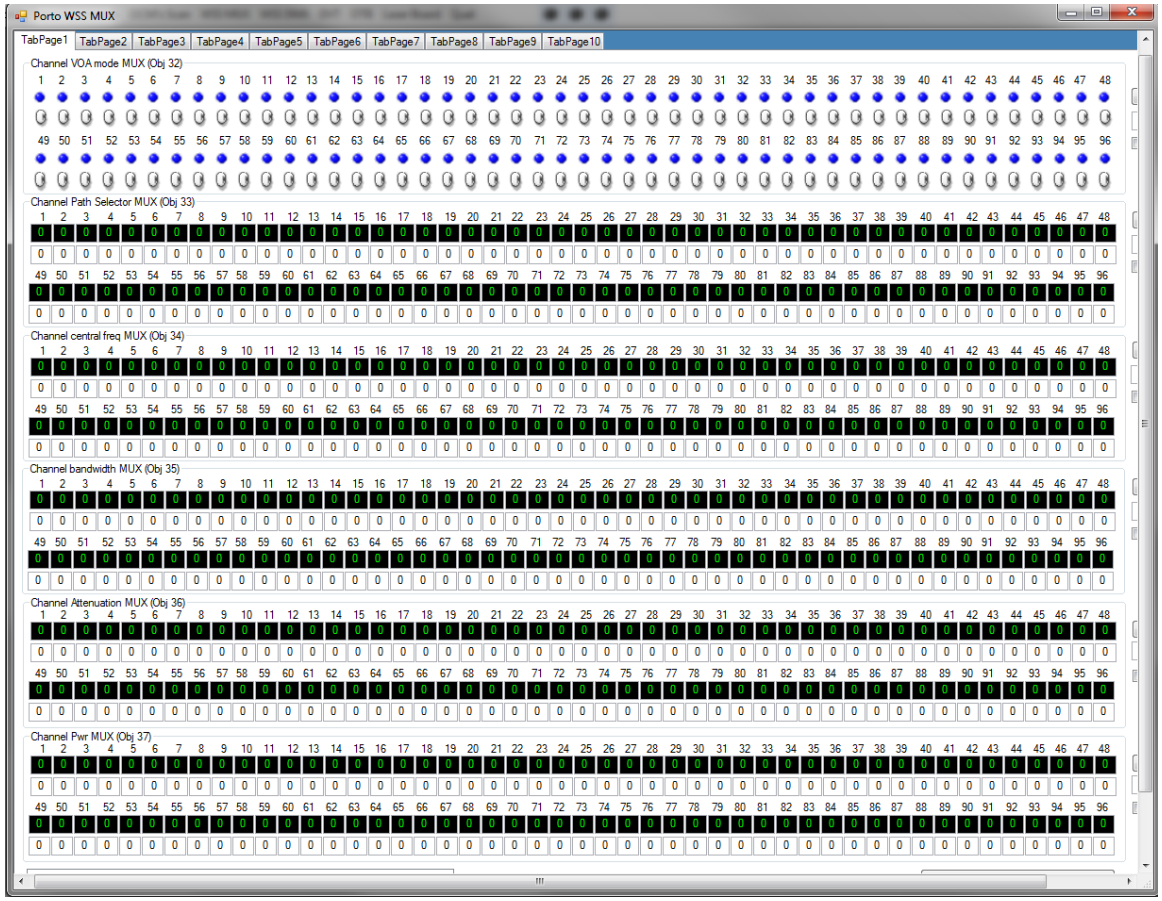

Figure 2.5 – FOX-C elastic channel definition panel, allowing each spectral slot to be individually addressed.

3 Switching and Filtering Sub-Channels within the Super-Channel Level

The optical processing hardware required to subdivide an individual pre-selected superchannel (by the fibre level WSS) to its constituent tributaries requires extremely fine optical resolution, beyond that demonstrated to date. The same hardware can also be used as a shaping filter at very high precision to target spectral forms. This is one unique aspect of the FOX-C project, which set out to demonstrate such capability at a target resolution of 1 GHz

over 200 GHz bandwidth (or free-spectral range) using an aggressive design of an arrayed waveguide grating (AWG).

The AWG for FOX-C is designed to provide extremely fine resolution, for accurate signal shaping and filtering, and broader bandwidth of operation to support entire super-channels. The AWG is implemented in a silica-on-silicon platform, using a 2% refractive index contrast for the waveguide definition. Waveguides are of 4×4 μm size, and 250 are used in the entire array. Design layout and actual AWG are shown in Figure 3.1.

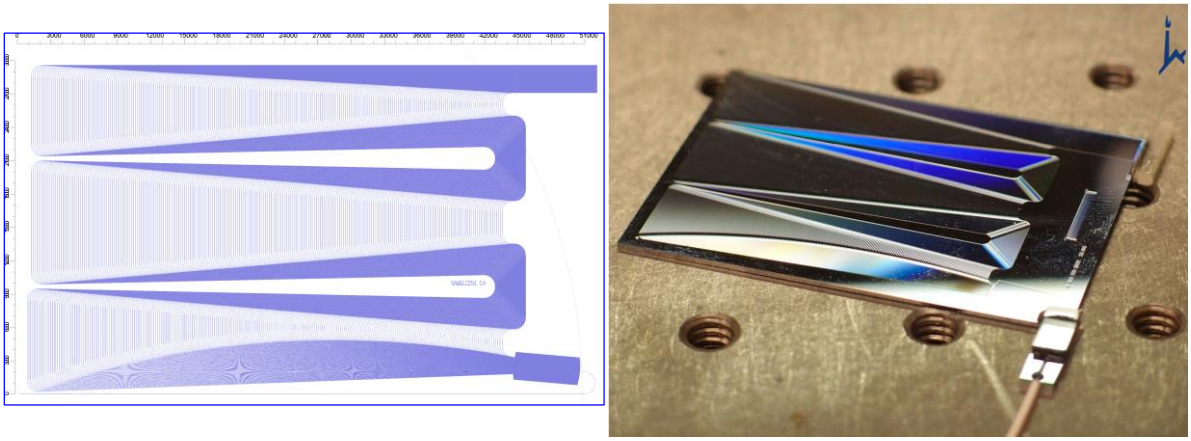

Figure 3.1 – AWG design and implementation for FOX-C. 200 GHz FSR and 250 waveguides should provide <1 GHz optical resolution, provided the AWG is devoid of phase errors.

Somewhat expectantly, the AWG performance is hampered by phase errors in the waveguide arms. This was to be expected as the maximal path length difference designed on chip is ~250mm! The phase errors recorded (Figure 3.2) show the output phase distribution appears nearly random, rendering this high resolution AWG useless unless this issue is addressed. Two such techniques are outlined next; one using a UV laser trimming technique to adjust the phases of the individual AWG arms; a second is based on an additional LCoS placed at the image plane, with the SLM imparting additional phase to correct for the distortion. These two techniques for correcting the phase errors are explained in the next sections. In addition to these correction techniques, we also launched an additional effort to achieve high-resolution optical filtering based on a large bulk diffraction grating. This system has been designed and is now being implemented.

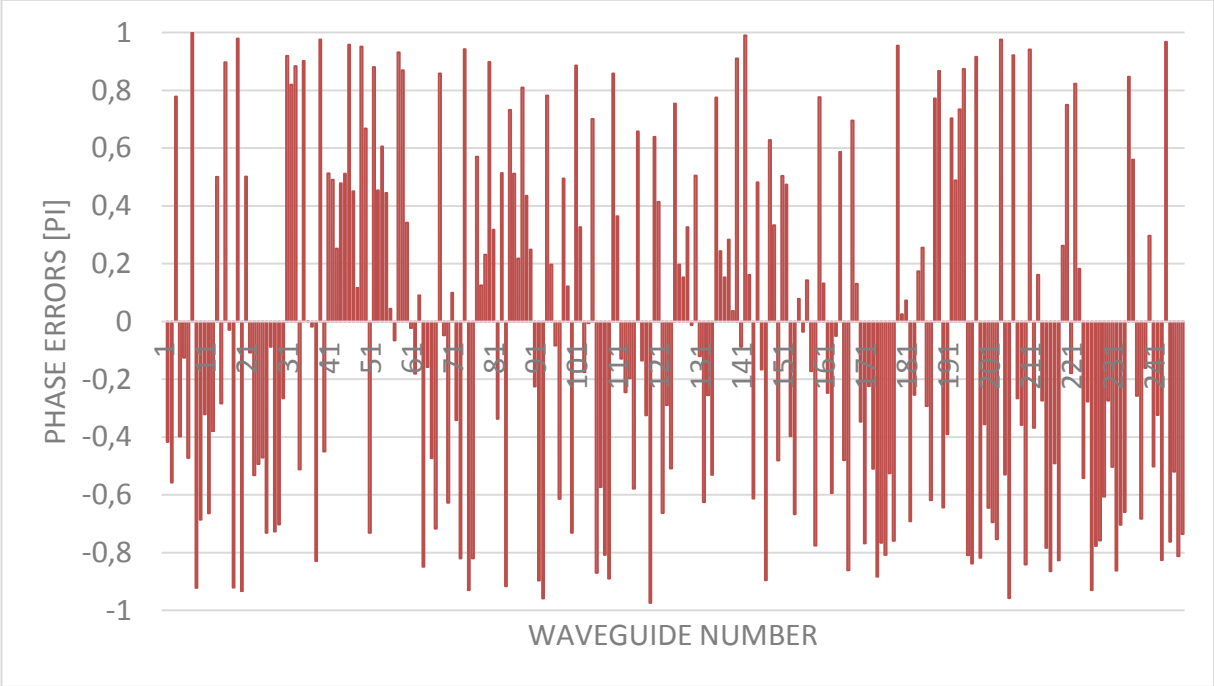

Figure 3.2 – Measured phase errors of 250 waveguide arms of high resolution AWG.

3.1 AWG Phase Error Trimming Using Intense UV Laser Irradiation

The phase errors at the AWG output facet stem mainly from deviations between the designed and fabricated waveguide geometry (dimensional accuracy), refractive index uniformity, and possible stress fields. All these deviation factors are uncontrolled to the level of accuracy required for the extreme resolution, and reflect directly on the waveguide's propagation constant, causing random accumulated differences in the optical paths, which account for the phase errors we measured.

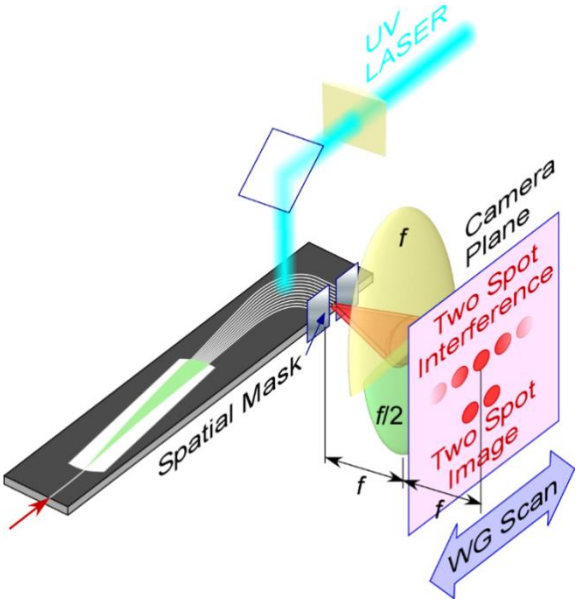

Figure 3.3 – Layout of the AWG phase error evaluation system and UV trimming. The UV beam scans along the waveguide arms and can expose each WG to a dose required to adjust the phase at the output.

One known method for compensating for AWG phase errors that is reported in the literature is based on the effect of photosensitivity. Under this effect, a germanium-doped silica waveguide experiences a local refractive index change under UV laser radiation (peak sensitivity at 244-248nm). This phenomenon is very successfully used in the writing process of fiber Bragg gratings. The UV laser illumination serves to alter the silicon-germanium chemical bonds in the glass matrix, locally resulting in higher packaging of the lattice and hence refractive index. This effect has finite refractive index change, $\Delta n \sim 10^{-3}$-10^{-4}, on account of the Ge doping. The photosensitivity effect can be enhanced by hydrogen loading the glass matrix (at very high H_2 pressure vessels) to $\Delta n \sim 10^{-2}$-10^{-3}, but the writing time is then limited due to hydrogen out-diffusion. In fiber Bragg grating writing, this diffusion time constant at room temperature is 1-2 days.

We decided to adopt the UV-induced photosensitivity effect for waveguide trimming using the experimental setup of Figure 3.3. In this setup the UV writing with a KrFExcimer laser (Coherent ExciStar) can be performed while the output phase is being continuously monitored in the near-infrared (NIR) camera. Targeting of the illuminated waveguide is performed by viewing through a dichroic mirror (reflects the laser's 248nm line). Initial experimentations with hydrogen loading were successful, but the out-diffusion time was 1-2 hours, since the waveguide is much closer to the atmospheric interface (about 15 microns away while in a fiber it is about 60 microns). Since the AWG has 250 waveguides that need to be trimmed individually, the writing is a lengthy process that cannot be completed within the out-diffusion timeframe.

Our experiments with UV radiation deposition on the waveguides revealed that we can get very large index shifts after lengthy illumination. This effect was analyzed and found to be stress-induced from the UV light absorption in the cladding resulting in local stress fields that modulate the phase. This effect can result in high phase modulation values (we exceeded 6π in experimental evaluation), and the phase modulation is not accompanied by amplitude modulation (or loss). Phase modulation using induced stresses required a level of control to balance the intensity (if the induced stress is too large the glass material ablates, and if is too small it requires lengthy writing). Attenuating the UV laser beam is also not simple, so in the end we resorted to increasing the illumination beam size (lowering the intensity, by mildly focusing to a beam size of ~300μm with an f=100mm lens) and exposing through a specially prepared metal mask (aperture of 2mm×100μm) that exposes a single waveguide (WG) at a time.

Experimental evaluation of the writing process is shown in Figure 3.4. The photosensitivity effect appears at the onset of illumination, but quickly saturates to a total phase change of 0.2π. This phase delay corresponds to an index change of $\Delta n = 8\times10^{-5}$(see Figure 3.4-left). The imaging system used to view the waveguide does not identify any change in the waveguide

image (before and after the brief illuminations). Upon prolonged exposure (the deposited UV energy is estimated by the number of UV pulses illuminating the sample), the phase delay increases monotonically to any desired phase lag value. This is due to the stress formed in the glass matrix. The image of the waveguide after the illumination appears different, scattering light from an expanded area defined by the mask. No change in transmission intensity was observed, hence the guided energy by the waveguide itself is not damaged in the process (no increased scattering or absorption).

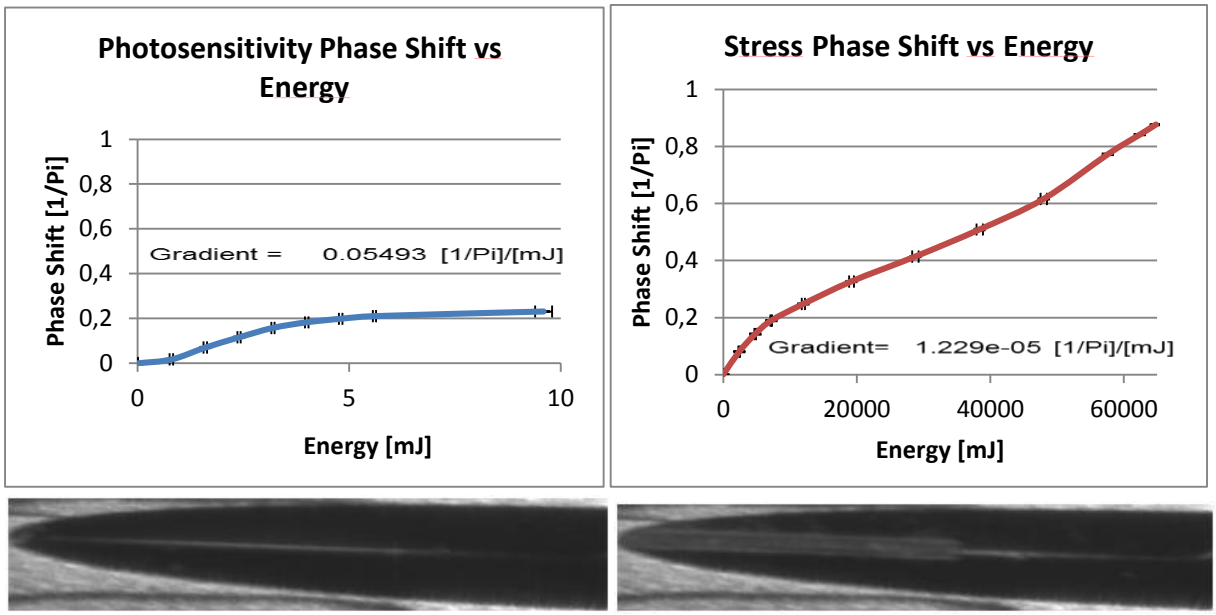

Figure 3.4 – Experimental phase trimming data. Top row:Phase shift as a function of energy exposure. Left shows photosensitivity phase shift; Right shows stress phase sensitivity. Bottom left: Image of WG (straight line) after photosensitivity trimming (image identical to untrimmed WG). Bottom right: Image of WG after stress trimming (visible due to deformation of PLC's surface).

The phase obtained by the stress gradient was found to be strongly polarization dependent (see Figure 3.5). This is explained by the phase gradient across the propagating mode being polarization dependent. On the opticalfiltering system implementation level this means that the AWG errors can only be corrected for a single polarization, and two AWGs working together in a polarization diverse scheme per fiber port will be required. To better understand the waveguide image obtained after UV irradiation (appearing wider under white light illumination for imaging), we measured the surface topography after the irradiation and found the surface swelled by 180nm over the illuminated aperture of width ~100 micron along a shape that looks Gaussian (see Figure 3.5-bottom). This surface topography is what we observe after illumination by an external white light source.

After mastering the phase trimming technique, we proceeded to phase trim a complete AWG. These experiments were performed on a smaller, test AWG (having a 25GHz FSR only, and 32 waveguides). After characterization of the phase errors at the output, the UV irradiation commenced, under feedback monitoring from the phase measurement technique.

The phases were trimmed such that at the output they are equal to within a small fraction of π; the far field radiation pattern from the AWG is focused to a spot (see Figure 3.6-top).

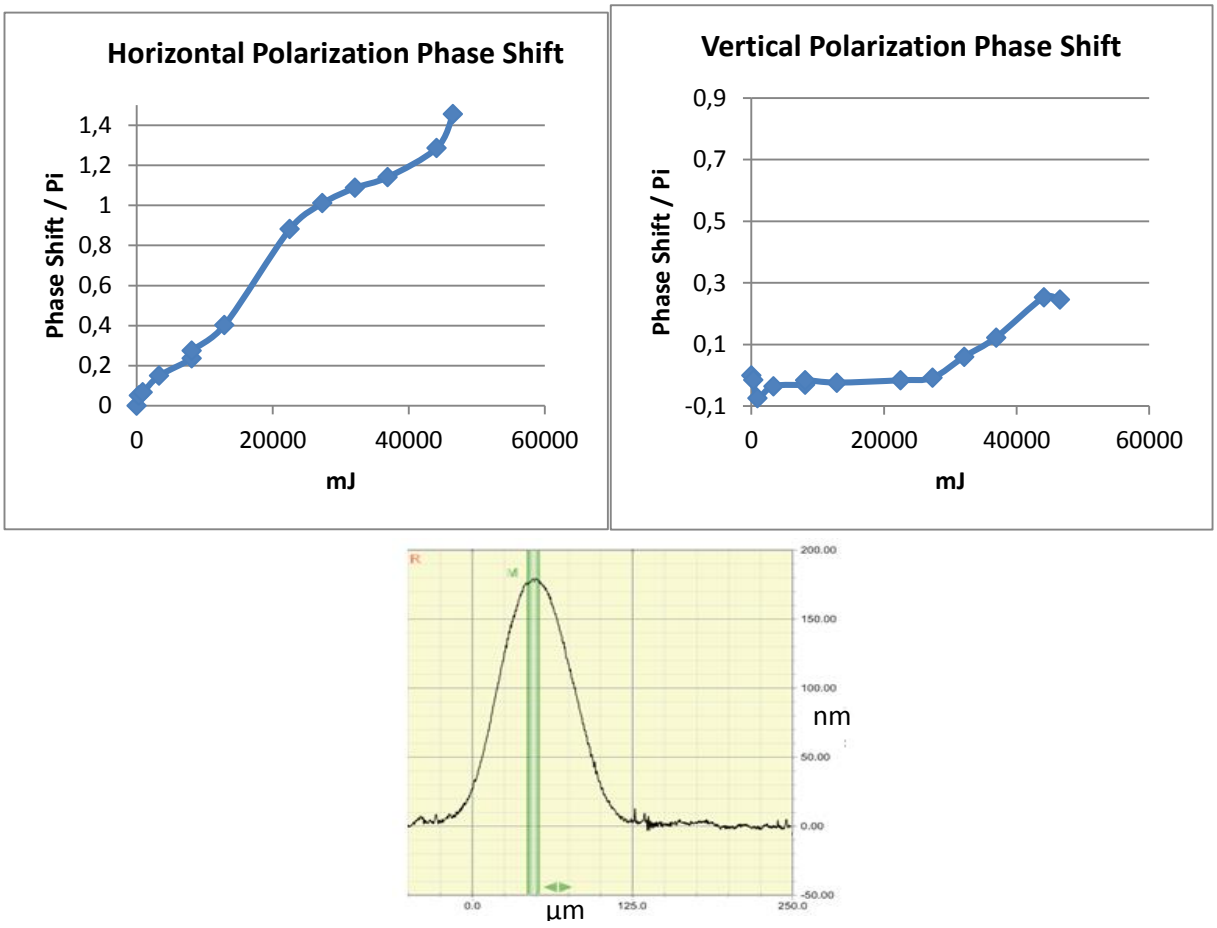

Figure 3.5 –Polarization-dependent phase trimming. Left: Horizontal polarization. Right: Vertical polarization. Bottom: Surface profile after trim obtained by Dektak profilometer.

However, two weeks later we found that the phase errors crept back in to the system to a small amount. The far field radiation pattern broadened, and a subsequent phase measurement revealed the increased phase error values (see Figure 3.6-bottom). During the two-week time, the AWG was dismounted from its vacuum chuck assembly and handled a bit. We attribute the phase error values creeping back in to stress relaxation, as the glass is a very viscous liquid and will relax stress on a slow time scale. This could have been exacerbated by the AWG global stress changing as the AWG was dismounted and remounted, with the AWG substrate conforming to the vacuum chuck planarity upon vacuum activation/deactivation. However this can still be directly related to a regular slow process of stress relaxation over time.

We are now working on ways to minimize stress relaxation, including bonding the AWG to a slab of CTE-matched Borosilicate glass glued to the bottom of the PLC to negate the vacuum effect on the stress (activation and deactivation), and provide greater rigidity to the AWG so that global stress would be held in check. We also introduced a vacuum regulator to maintain

steady and lower vacuum levels on the AWG assembly and thus improve repeatability from one trimming session to another.

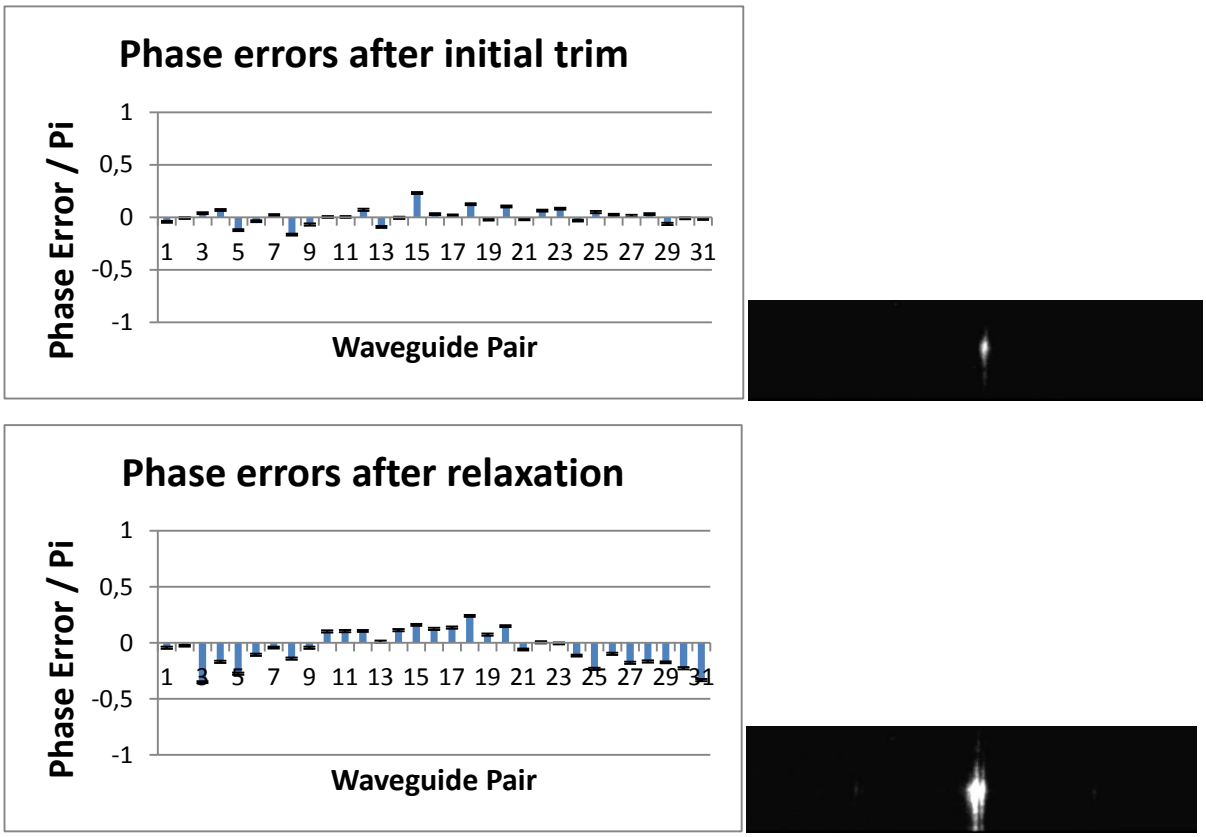

Figure 3.6 – AWG phase trimming results. Top row: Directly after trimming session; output phase errors are nearly uniform and we witness the far field radiation constructively focusing. Bottom row: After two weeks; output phases drift and far field radiation pattern is broadened.

The applied measures to better control stress and the remaining stress relaxation processes are currently under investigation to better understand if this technique is viable. We also contemplated performing the UV laser trimming in a hydrogen environment, so that a greater photosensitivity effect comes into play, however the safety concerns of such an arrangement are impractical (making the setup explosion proof). Alternatively, we realized an optoelectronic phase compensation technique based on phase modulation with anSLM, as explained next.

3.2 AWG Phase Error Correction with a Spatial Light Modulator

An alternative to the UV phase trimming solution is using a second LCoS phase modulator to introduce the additional phases onto the AWG output. The experimental setup comprises two parts (see Figure 3.7): First, a telescopic imaging stage in order to magnify the waveguides and efficiently fill the LCoS SLM. Second, after applying the phase correction, a spatial Fourier transform with a lens to obtain a spatially dispersed signal where a second SLM is placed for

spectral modulation. The signal is then back-propagated through the system to the AWG and separated with a circulator.

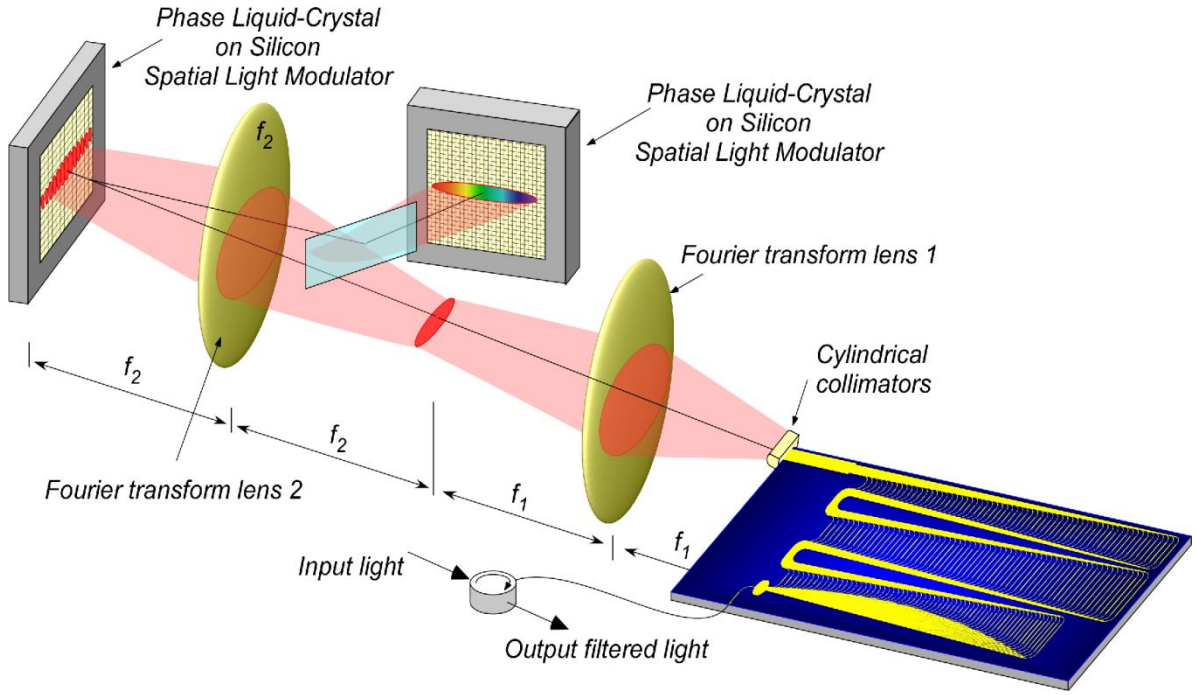

Figure 3.7 – Experimental setup for compensation of AWG phase errors with an LCoS phase modulator and spectral processing in the Fourier plane.

The implementation of the imaging section proved a little challenging. The near maximal magnification that can be imaged is a factor of three, since the waveguide array is 250×18μm=4.5mm wide, which after magnification reaches 13.5mm, which is nearly the LCoS width (1920×8μm=15.36mm). This magnification ratio can be obtained with a 50mm and 150mm lens combination. The problem we encountered was the imaging quality due to the large field of view. The imaging is assessed by placing a NIR-sensitive camera at the image plane of the AWG. We initially used a 150mm stock ThorLabs lens in the setup but the image suffered from field curvature preventing sharp focusing across the field (the camera could be positioned forwards/backwards to make the center or edges of the image come into focus, but never both).

We first tried to resolve this with alternative optics (a telescope with infinity corrected lens of 40 and 100 mm focus lengths, for a magnification factor of 2.5, i.e. smaller field). Large magnification of the AWG output is important as the spatial resolution of the LCoS is also limited. The 40 and 100 mm telescope proved unsatisfactory because of inadequate working distance which caused extremely high coupling losses. Then we obtained a custom 150mm lens from a different source, which was capable of focusing across the field with minimal aberrations. This was the best choice though it took some time to learn how to properly work with the imaging arrangement (see Figure 3.9-left).

Next, the first LCoS SLM is placed at the image plane and the camera is moved to the Fourier plane (see Figure 3.8). The first task is to identify the WG positions striking the LCoS. This is accomplished by column scanning across the SLM, directing light to the camera, and registering the power. The resulting power vs. column reveals the WG positions (Figure 3.9).

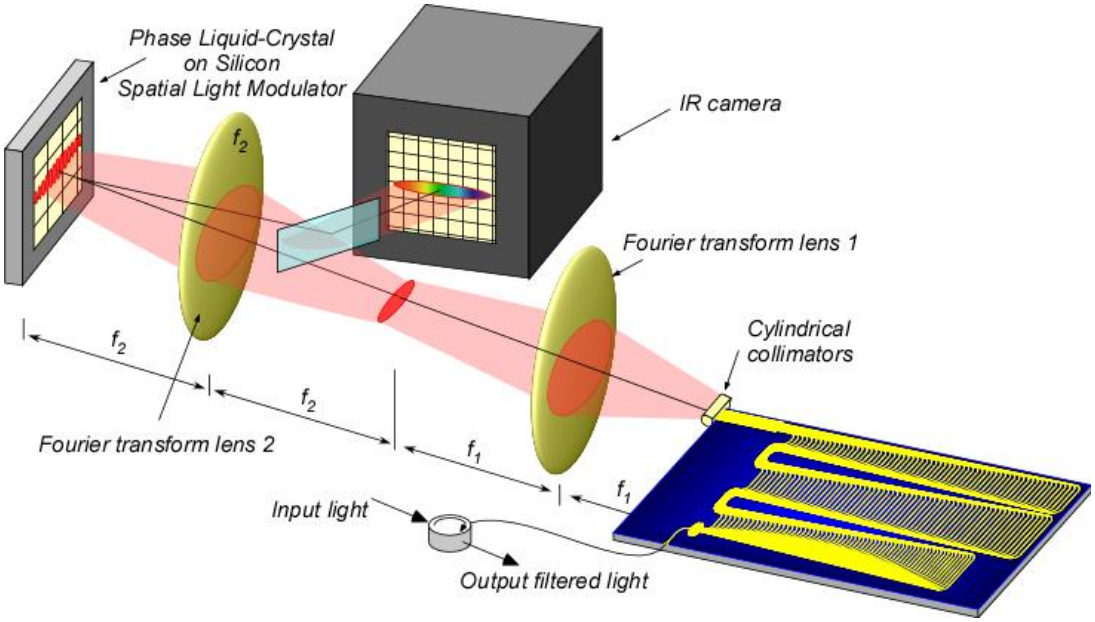

Figure 3.8 – The placement of the camera in the experimental setup for locating WGs and conducting interference between adjacent WGs.

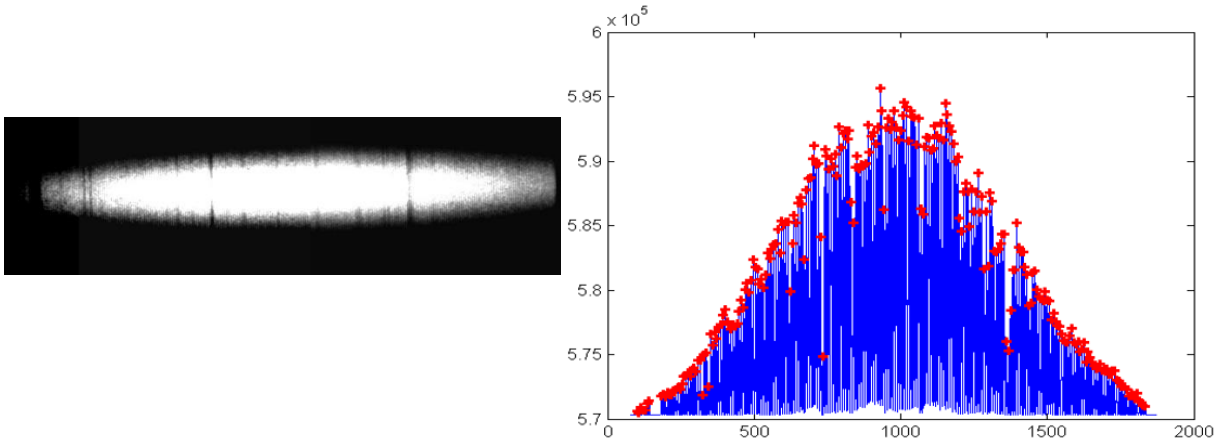

Figure 3.9 – Waveguides at the image plane. Left: Direct image of the waveguide array. Right: Identification of the WG positions by column scanning across the array. Correspondence with image is apparent (identified by dead waveguides).

Once the waveguides' locations are known, the procedure to correct the phase errors begins. This is accomplished by observing the interference pattern in the Fourier plane (where the IR camera is still present) for each contiguous waveguide pair. To select the waveguide pair, a linear phase is applied to the image of the two waveguides, causing them to tilt away from the rest upon reflection. The relative phase of one waveguide is scanned with respect to the other one and from the observed far-field interference pattern it is easy to identify when the waveguides are in phase (due to the symmetry in the interference pattern, see Figure

3.10). Thus by scanning across the array, the entire relative phase error map is obtained across the array. These corrective phase values are stored in memory, and after the pair-wise scanning procedure is complete they are applied to all 250 waveguides in the array (see Figure 3.11). Each WG illuminates 7 pixel columns, over which the phase values are encoded.

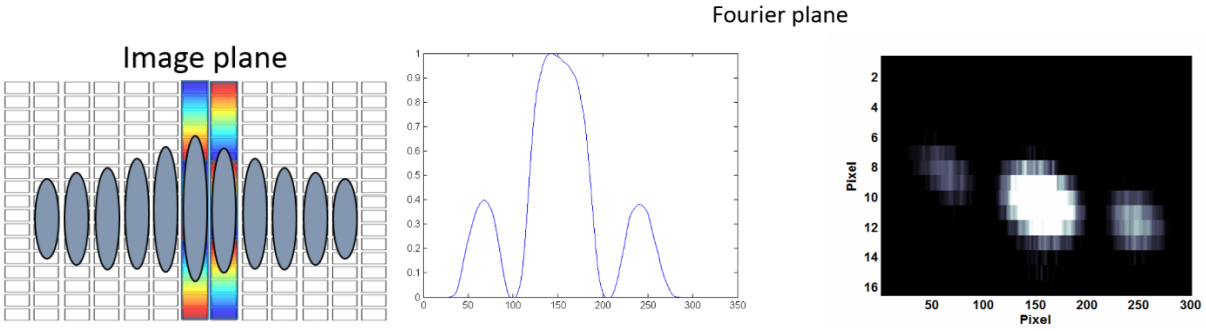

Figure 3.10 – Left: Image plane illustration of two adjacent waveguides tilted on the SLM to direct the light from only those two WG, while one has an applied phase offset.Right: Photo of two in phase waveguides.Center: A vertical sum of the image intensity on the camera.

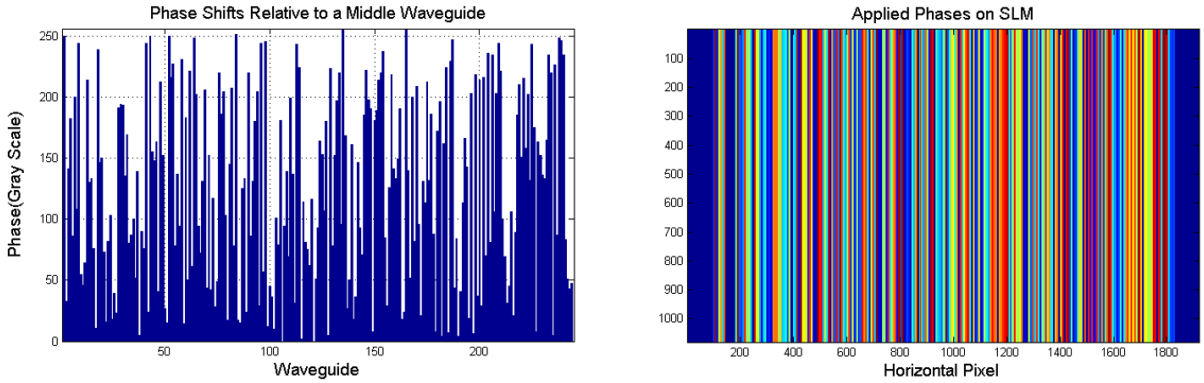

Figure 3.11 – Left: All WG phases compared to a middle WG in gray scale.Right: The color-coded HDTV image frame sent to the SLM (actual values are greyscale) to phase synchronize the AWG. Colors (from blue to red) represent greyscale values from 0 to 255.

To ascertain the phase corrections are indeed all fully synchronized, we now observe the far-field interference pattern of the entire array with the camera in the Fourier plane when introducing a CW laser. Prior to the application of the phase corrections, the observed far-field image resembles a speckle pattern from the random phases:

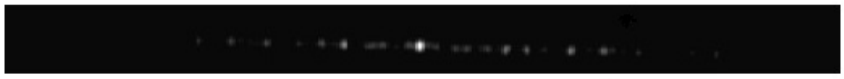

With the full phase compensation applied across the entire array, we see the constructive interference at the main diffraction lobe, as well as the adjacent orders (as the waveguide array is a sampled source):

This confirms that the AWG is properly phase corrected.

The final step in setting up the filtering apparatus is to place the second LCoS SLM at the spectral plane (instead of the NIR camera), for performing spectral manipulation experiments. Various filtering functions can now be applied at the Fourier plane and back reflected to the AWG. The spectral filters observed indeed confirm the extremely sharp filter characteristics (Figure 3.12). To properly assess their fine resolution, a swept laser characterization must be employed as an optical spectrum analyzer does not have sufficiently fine resolution. The measured transitions from pass to block band (90:10 or -0.5dB to -10dB) occur over a bandwidth of 0.8 GHz, exactly matching the AWG design specs. This confirms that this phase correction technique operates well, and validates the AWG design. The complete system can be seen in Figure 3.13.

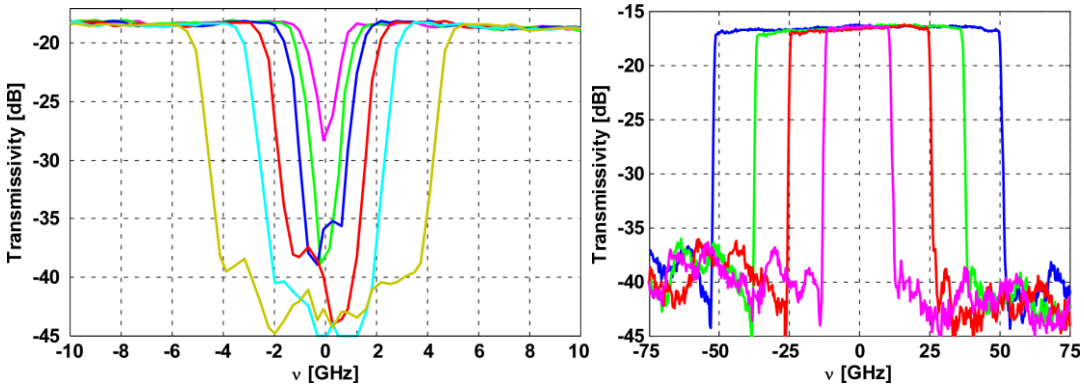

Figure 3.12 – Measured fine spectral filter performance characteristics, when variable bandwidth channels are deployed at spectral granularity of 100 MHz and a record optical resolution of 0.8 GHz.

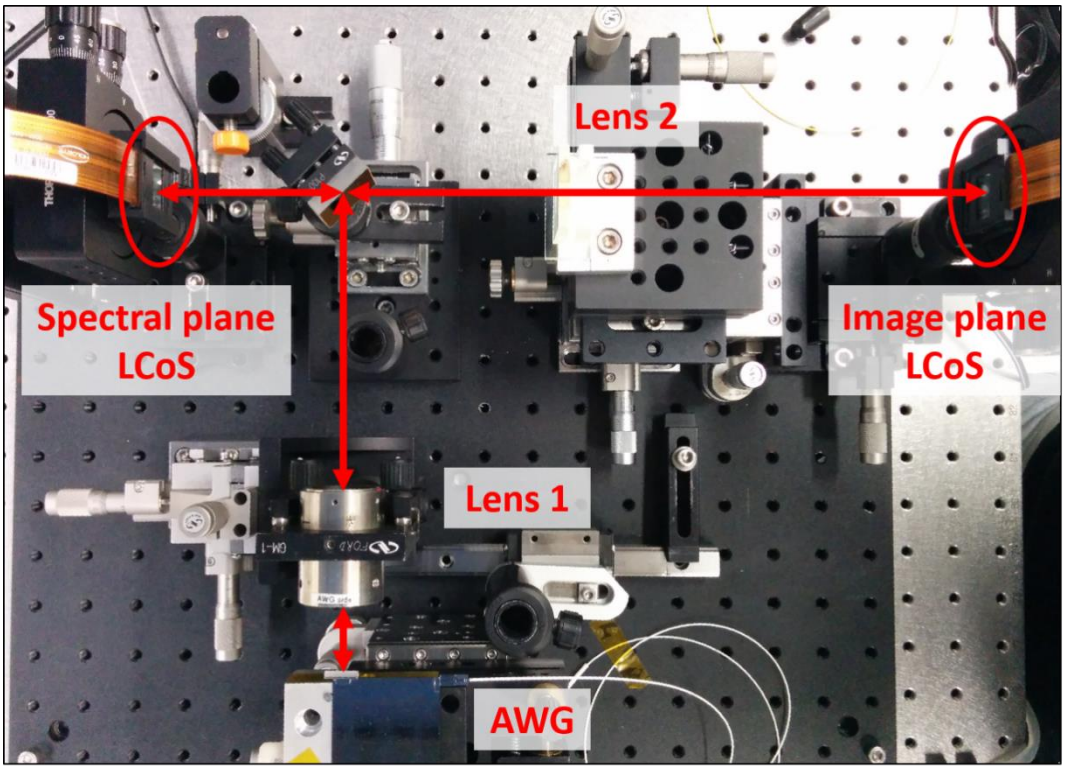

Figure 3.13 – Top view of experimental system for fine resolution optical filtering using the dual LCoS approach.

Moving forward, we still need to introduce two more elements to complete the filter system. First, a polarization diversity scheme needs to be introduced to make the filter polarization insensitive. Following that, a second AWG will be added (as a second layer on top of the first AWG) to offer a two port switching arrangement.

3.3 Bulk Grating based Fine Resolution Filter

As an alternative filter design to the AWG based systems described above, a bulk grating based filtering apparatus effort has been launched. In the earlier stages of the research (reported in D4.1), we established the theoretical requirements from such a diffraction grating approach. To maximize the resolution, it is desirable to have both incident and diffracted beams (Littrow mounting) strike at grazing incidence to maximize the illumination area.

After studying various potential grating options, we identified Echelle gratings as a viable option. The grating that appeared most suitable is a 31.6 gr/mm grating operating in the 40th order (equivalent to a 1264 gr/mm grating). The Littrow mounting angle in this case is 77.7°, and in order to obtain ~1.5GHz resolution a ruling size of 200mm is required. Since the Littrow angle is so close to grazing, this also sets a minimum Fourier lens focal length of ~100mm (as the grating is positioned in the back focal plane and requires a large working distance). The grating simulated performance (performed by Richardson Grating Lab) is shown in Figure 3.14. This grating is highly efficient for the orthogonal incidence polarization state (S polarization), and hence will necessitate using conventional polarization diversity to render the system polarization insensitive (which is also required due to the LCoS SLM).

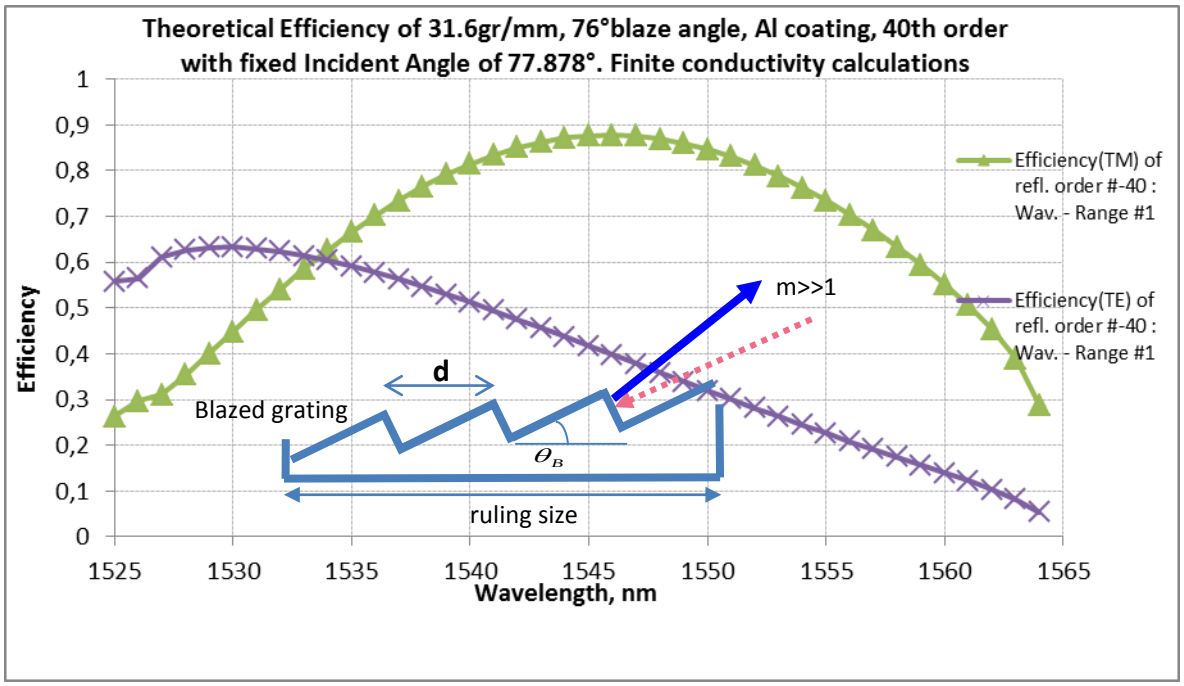

Figure 3.14 – Expected diffraction efficiency of Echelle grating operating in 40th order.

The optical system design to utilize this grating is required to illuminate the grating with a beam of size ~15mm (which will illuminate the entire grating due to the grazing incidence). Hence, special anamorphic beam preparation is required to fully utilize this grating to keep total system height reasonable. With a free-space based design we can also fully utilize the third dimension (height) and implement a multi-port switch. A 1×2 switching functionality can be implemented for the ROADM sub-channel extraction and insertion function. In addition, we can also pack two independent 1×2 switched by an angular separation in the height direction (similar to dual WSS implementations). The complete optical design we envisage can be seen in Figure 3.15.

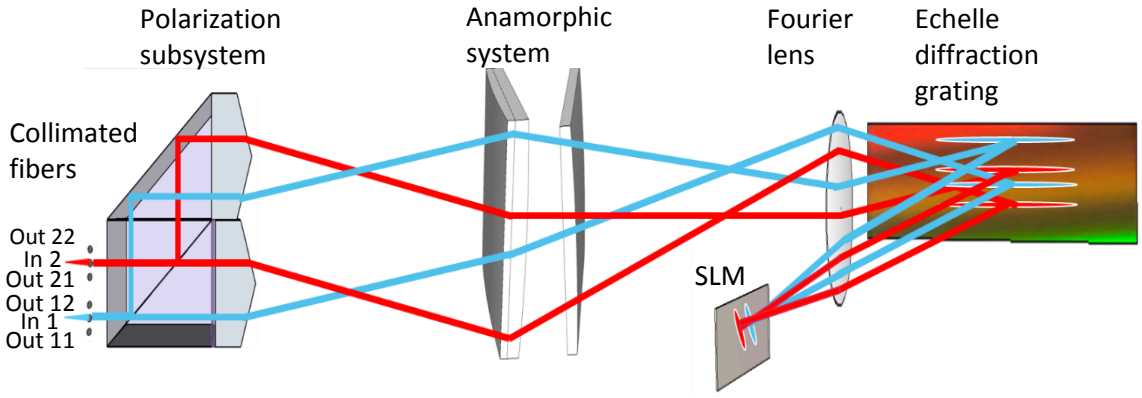

Figure 3.15 – High resolution filter, employing blazed Echelle grating for high resolution dispersion and an LCoS switching engine. The LCoS SLM can be reprogrammed to allocate optical channel bandwidths differently at quanta determined by the spectral granularity.

The switch is comprised of two major subassemblies:

- The role of the first subassembly is to image the input and output optical fiber end faces onto a common magnified spot with an anamorphic beam ratio, and to convert the distinct spatial locations of the fibers to unique angular propagation directions at the spot position.

- The second subassembly uses a lens and a diffraction grating in a spectrographic arrangement to spatially disperse the input magnified common spot and finely resolve the channels onto the phase LCoS SLM, such that each channel is imaged upon a separated area on the SLM for independent addressing.

Due to the strong angular dispersion and the long lens focal length (to be implemented at f=120mm), the bandwidth support will be only ~20nm due to the finite extent of the LCoS aperture (with additional bandwidth limitation imposed by the grating efficiency curve). This is of course better than the case of the bandwidth limitation of the AWG FSR. An anamorphic system was designed to create a 1:50 ratio. This is an aggressive design which has never been attempted before, brought about by the high resolution needs and the requirement to keep the system relatively small. The beam size in the spectrally dispersed plane is designed to be 700μm×13.5μm.

Both the phase SLM and the diffraction grating are polarization sensitive elements, requiring a polarization diverse design that will ensure single polarization operation inside. A PBS will be used since it can also serve as platform which creates the two switches internally with bi-angle prisms that will be attached to the PBS face applied to each polarization. Thus each fiberbeam is divided to two separate beams that are parallel and set to the same polarization, and each switch is tilted to a unique propagation direction for spatial separation.

A full ZEMAX optical performance simulation of the system has been run. The simulation helped to decide which anamorphic system will fit system goals, and also helped optimizing the data of the optical components, in order to maximize the resolution with minimal losses.The system simulation takes into consideration 2 input fibers- each directs data to 2 different output fibers, each is split to 2 polarizations. 3 different wavelengths are available, i.e. there are 24 possible configurations in the system. The ZEMAX simulation predicts that the aggressive anamorphic ratio can be delivered by the lenses. The optical setup provides very similar performance metrics for each polarization, which should minimize PDL.

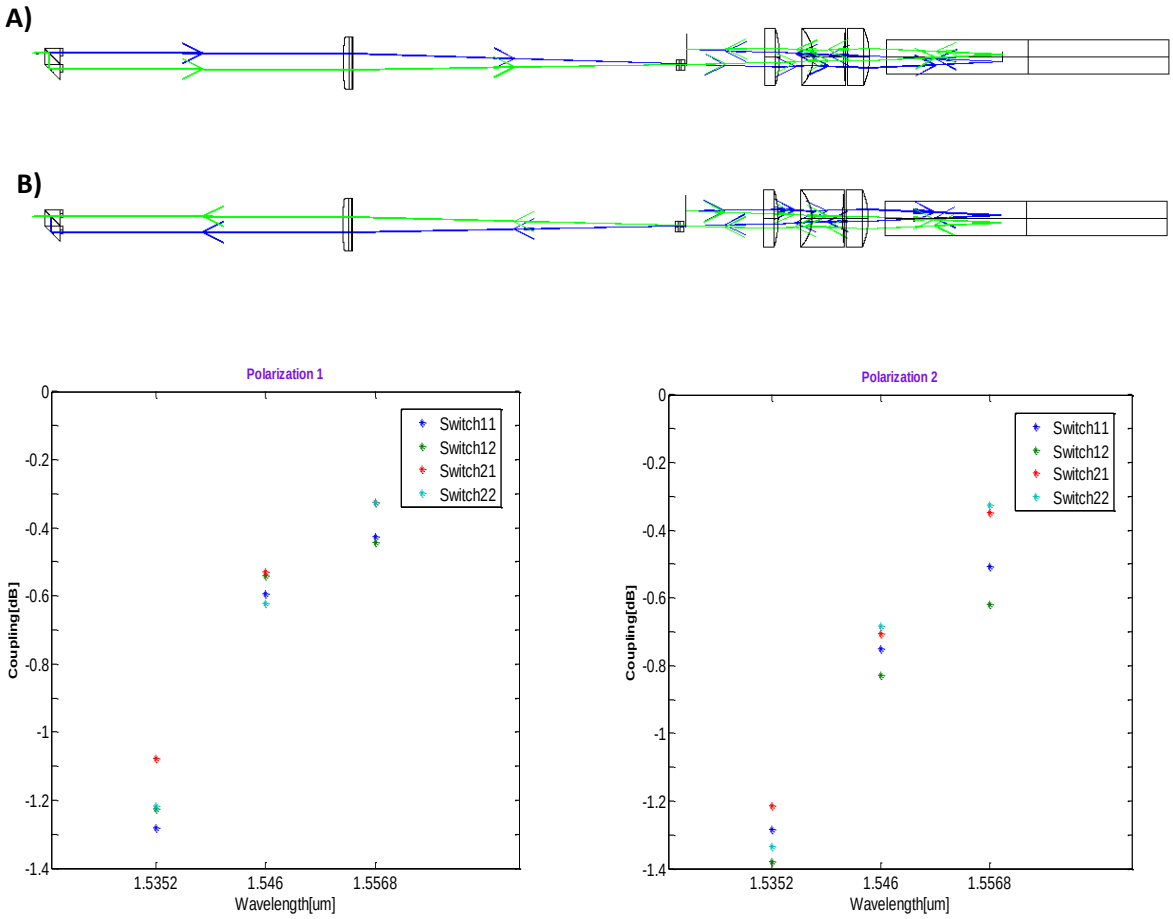

Figure 3.16 – The ZEMAX optical system simulations. A.Rays from a single input fiber to the SLM, B. Rays from the SLM to a single output fiber.Bottom: Coupling performance evaluated for each polarization.

4 Conclusions

This report accompanies the developed hardware elements required to implement the 'Drop' functionality of the FOX-C hierarchical ROADM. Partner Finisar has implemented a fiber-level WSS for switching super-channels using a flexible grid assignment with accompanying control elements. Partner HUJI has developed a fine-resolution optical filter for sub-channel Add/Drop from the separated super-channels based on the AWG with optoelectronic phase compensation. In addition, a high-resolution free-space variant of a WSS has been designed, and will be constructed by the end of the project's second year. A table summarizing the specifications of these Fox-C 'Drop' elements appears below. These 'Drop' component elements represent the state of the art achievable in optical networking today, and will be utilized for system experiments in the project's second half.

	Finisar Flex-WSS	**HUJI AWG filter**	**HUJI grating filter***
Operation wavelength range	C-band (1528.8-1566.7 nm)	Any contiguous 200 GHz band	~20nm within the C-band
Spectral addressability	6.25 GHz	100 MHz	~150 MHz
Optical Resolution	7.5 GHz	0.8 GHz	1.5 GHz
Insertion loss	<5 dB	~15 dB	TBD

* The values for the fine-resolution bulk grating filter are design values, as this switch variant is yet to be built.